

A linear model for chirp-pulse microwave computerized tomography: applicability conditions

A M Massone¹, M Miyakawa², M Piana³, F Conte⁴ and M Bertero^{5,6}

¹ CNR-INFM, LAMIA, Via Dodecaneso 33, I-16146 Genova, Italy

² Center for Transdisciplinary Research, Niigata University, Niigata, Japan

³ Dipartimento di Informatica, Università di Verona, Ca' Vignal 2, Strada Le Grazie 15, I-37134 Verona, Italy

⁴ Dipartimento di Fisica, Università di Genova, Via Dodecaneso 33, I-16146 Genova, Italy

⁵ Dipartimento di Informatica e Scienze dell'Informazione, Università di Genova, Via Dodecaneso 35, I-16146 Genova, Italy

Received 9 March 2006, in final form 11 October 2006

Published 27 October 2006

Online at stacks.iop.org/IP/22/2209

Abstract

Chirp-pulse microwave computerized tomography (CP-MCT) represents an innovative medical imaging technique. One of the advantages of CP-MCT is that data reduction is based on the standard algorithm of x-ray tomography, namely filtered back-projection and therefore is very fast, even if not very accurate. For this reason we recently proposed a modification of this algorithm based on a linear model, hence on a computationally efficient approach. The method has been validated by means of real data obtained with the Niigata prototype of the CP-MCT scanner. However, the applicability of the underlying model has not yet been completely analysed. In this paper, we first investigate the assumptions leading to the linear model and then we show, by means of numerical simulations, that it can provide quantitative maps of the attenuation constant of the body in the low-contrast case.

1. Introduction

Chirp-pulse microwave computerized tomography (CP-MCT) is a multi-frequency approach in microwave tomography [1–4], developed at Niigata University, in order to perform non-invasive thermometry of the human body via the temperature dependence of the microwaves' attenuation through the biological tissues. This imaging modality is essentially based on the following approach.

An antenna S (source) emits a chirp pulse with a frequency in the range of 1–2 or 2–3 GHz and a sweep time between 20 and 200 ms. The pulse crosses the body and is detected by a second antenna R (receiver). Part of the input signal of S is multiplied in the time domain by the output signal of R and this mixed signal is passed through a Fourier filter

⁶ Author to whom any correspondence should be addressed.

to extract the amplitude of the Fourier component corresponding to the beat frequency. This technique, known as *microwave time delay spectroscopy* (MTDS) [5], is used for selecting the signal propagating along the straight line S–R, hence reducing diffraction effects and improving resolution.

The source S and the receiver R move along two parallel guides which can rotate a given angle at the end of the process. Therefore, the scanning geometry is similar to that of parallel beam x-ray tomography. The amplitudes of the beat components for all S–R positions are the raw data of CP-MCT.

After appropriate processing of these raw data, the result of linear scanning with a given angle provides a CP-MCT projection of the body, and the set of these projections is the CP-MCT sinogram. Next, by implicitly assuming an absorption model similar to that of x-ray propagation, these projections are treated as the Radon projections of the body, and image reconstruction is performed by means of the classical *filtered back-projection* (FBP) algorithm for Radon transform inversion.

In principle, CP-MCT is supposed to be an effective microwave imaging technique, involving all the advantageous features of microwave tomography (low invasivity and optimality in contrast) and exempt from its most typical drawbacks, such as strong diffraction effects and low spatial resolution. Furthermore, the analogy with a well-known and well-established modality such as x-ray tomography is appreciated and the low computational demand makes CP-MCT a potential candidate for medical applications. A comparison of CP-MCT with another microwave modality is discussed in [6].

In spite of good results obtained with different kinds of phantoms [4], the CP-MCT images are still affected by a considerable blur due to incomplete discrimination of the straight path joining the two antennas and to their finite aperture size [7]. Moreover, it is not completely clear what the physical parameter imaged by CP-MCT is.

An analysis of these limitations should imply accurate mathematical modelling of the CP-MCT modality, but such a task is quite difficult as one can easily understand by taking into account the different steps of the imaging procedure. Indeed, it implies not only microwave scattering but also mixing and filtering of the detected signal, as required by MTDS.

An attempt to develop an improved ‘empirical’ model was made in a series of papers [7–9]. According to this model, a CP-MCT projection is given by a blurred version of the corresponding Radon transform, the blurring being described by an appropriate *point spread function* (PSF). This description of the signal propagation/detection in the scanner naturally inspires a two-step reconstruction algorithm, where the first step is the regularized deconvolution of the CP-MCT sinogram and the second step is the filtered back-projection of the deconvolved sinogram.

The aim of the present paper is twofold: first, to clarify what the physical parameter that is imaged in CP-MCT is and, second, to understand the conditions to be satisfied by this parameter to allow the use of the linear model.

For this purpose we formulate explicitly the very crude assumptions and approximations underlying the linear model. If they are satisfied, then we show that the CP-MCT images are maps of the attenuation constant of the body or, more precisely, of the contrast between the attenuation constant of the body and that of the bolus surrounding the body. As a consequence, in the case of exact discrimination of the signal propagating along the path joining the two antennas, the CP-MCT projections coincide with the corresponding Radon projections of the contrast function. Moreover, residual diffraction effects and finite antenna aperture are taken into account by the ‘blurred’ version of this projection, that is described as the convolution of the Radon projection times the PSF of the scanner, defined as the CP-MCT projection of a small body located in the centre of the imaging region.

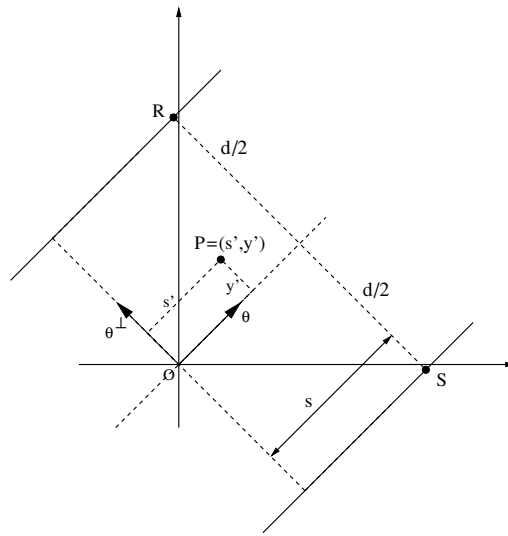


Figure 1. The scanning geometry in CP-MCT. S and R denote the source and the receiving microwave antennas, respectively, and P is a point in the imaging domain.

This explicit model, described in section 2, is essentially a systematization of a number of assumptions more or less implicitly used in our previous papers. It implies several consequences that can be tested in a simulation study which is briefly described in section 3. The main results are given in section 4 where we show that the linear model can be successfully used at least in the case of objects with a simple geometry and a contrast with respect to the bolus not exceeding 30%. More precisely, in the case of bodies characterized by a low contrast in the attenuation constant, CP-MCT combined with our linear model can provide quantitative maps of this electrical parameter. The imaging of high-contrast bodies is a completely open problem.

2. Modelling of CP-MCT raw data

As we pointed out in the introduction, CP-MCT and x-ray tomography are characterized by several common features. In particular, the geometry of the CP-MCT prototype operating at Niigata University is the same as that of traditional x-ray scanners in the parallel beam set-up (CP-MCT scanner with fan beam geometry is nowadays under development [10]). In such a case it is possible to reduce the problem to a 2D one if we consider objects approximately invariant with respect to translations in the direction of the rotation axis and TM-polarized electromagnetic fields generated by line sources.

The coordinate system we use in the imaging plane is defined in figure 1, where $\{\theta, \theta^\perp\}$ is a pair of unit vectors, with θ orthogonal to the straight line S–R. Therefore, the coordinates of this line are given by (s, θ) . By moving the two antennas along the direction θ we get the raw data providing the CP-MCT projection in this direction.

We denote by $u(s, y'; \omega)$ the component of the electric field, orthogonal to the imaging plane and corresponding to a given frequency ω ; it is a solution of the Helmholtz equation

$$\Delta u(\cdot; \omega) + k^2 u(\cdot; \omega) = 0, \tag{1}$$

where k is the complex wavenumber which, in general, depends both on the frequency ω and on the position P . It is given by

$$k^2(\omega; P) = \frac{\omega^2}{c^2} \left[\epsilon(\omega; P) + i \frac{\sigma(\omega; P)}{\epsilon_0 \omega} \right], \quad (2)$$

where ϵ and σ are, respectively, the permittivity and conductivity of the medium.

A first approximation consists of neglecting the frequency dependence of these parameters in the frequency range between 1 and 3 GHz. Moreover, we will assume that the following quantity

$$\eta = \left(\frac{\sigma}{\omega \epsilon_0 \epsilon} \right)^2 \quad (3)$$

is sufficiently small in the same frequency range. If we put

$$k(\omega; P) = \beta(\omega; P) + i\alpha(\omega; P), \quad (4)$$

where α and β are the *attenuation constant* and the *phase constant*, respectively, then, at the first order in η , we have (see [8])

$$\alpha(\omega; P) = \frac{1}{2} \sqrt{\frac{\mu_0 \sigma^2}{\epsilon_0 \epsilon}} \left\{ 1 - \frac{1}{4} \eta \right\}, \quad \beta(\omega; P) = \frac{\omega}{c} \left\{ 1 - \frac{1}{8} \eta \right\}, \quad (5)$$

where $c = (\epsilon_0 \mu_0 \epsilon)^{-1/2}$ is the phase velocity of the microwave in the medium. Therefore, in the limit $\eta = 0$, both the attenuation constant and the phase velocity do not depend on the frequency.

In view of introducing the absorption model, we first consider a homogeneous medium (the bolus) and a plane wave propagating in the direction θ^\perp and modulated by the chirp signal

$$c(t) = A \chi_S(t) \sin \left(\omega_1 t + \frac{1}{2} K t^2 \right), \quad K = \frac{\omega_2 - \omega_1}{T_S}, \quad (6)$$

where T_S is the *sweep time* of the signal and $\chi_S(t)$ is the characteristic function of the interval $[0, T_S]$. Then, if we denote by $u_\theta(y'; t)$ the component of the electric field of this plane wave, we have

$$u_\theta(y'; t) = \frac{1}{2\pi} \int_{-\infty}^{+\infty} \hat{c}(\omega) e^{-i(\omega t - k_b y')} d\omega, \quad (7)$$

where $\hat{c}(\omega)$ is the Fourier transform of the chirp signal and k_b is the complex wavenumber of the bolus, given by equation (2) with $\{\epsilon, \sigma\}$ replaced by $\{\epsilon_b, \sigma_b\}$. In a similar way, we denote by α_b and β_b the attenuation and phase constants of the bolus.

In the case of a homogeneous medium, the electrical parameters do not depend on the point P . Therefore, if we insert equation (5), for α_b, β_b , with $\eta = 0$, into equation (7), we find that, at a distance d from the origin, the plane wave is given by

$$u_\theta(d; t) = e^{-\alpha_b d} \frac{1}{2\pi} \int_{-\infty}^{+\infty} \hat{c}(\omega) e^{-i\omega(t - \frac{d}{c_b})} d\omega = e^{-\alpha_b d} c(t - T_D), \quad (8)$$

where c_b is the phase velocity of the bolus (also independent of ω) and $T_D = d/c_b$ is the time delay of the wave front travelling from $y' = 0$ to $y' = d$.

During the time interval $[T_D, T_S]$, the signal at the exit of the mixer is given by $S(t) = c(t)u_\theta(d; t)$ and it is easy to see that it contains the beating term (see [7]):

$$S_B(t) = \frac{1}{2} e^{-\alpha_b d} A^2 \chi_S(t) \cos \left(K T_D t + \omega_1 T_D - \frac{K}{2} T_D^2 \right), \quad (9)$$

where we have identified the interval $[T_D, T_S]$ with the interval $[0, T_S]$ since $T_D \ll T_S$.

The modulus of the Fourier transform of this beat term shows two peaks at $\omega = \pm\omega_B$, where $\omega_B = KT_D$ is the beat frequency; moreover, in the neighbourhood of ω_B , it is approximated by

$$|\hat{S}_B(\omega)| = \frac{1}{2} e^{-\alpha_b d} A^2 \frac{T_S}{2} \left| \text{sinc} \left[\frac{T_S}{2} (\omega - \omega_B) \right] \right|, \quad (10)$$

with a maximum value M given by

$$M \simeq \frac{1}{2} A^2 \frac{T_S}{2} e^{-\alpha_b d} = C e^{-\alpha_b d}, \quad (11)$$

where C is a constant that *does not depend on the properties of the medium*. This is the output of the filter in the simplified case of a plane wave in a homogeneous medium.

Let us consider now the general case of a body immersed into a bolus and let us denote by $M_\theta(s)$ the output of the filter, corresponding to the (s, θ) -configuration of the two antennas. The antenna S is emitting a chirp signal and we assume that, along the straight line joining the two antennas, the field can be locally approximated by a plane wave that is attenuated in the way described above. Then, one can assume the following simplified absorption model for $M_\theta(s)$:

$$M_\theta(s) = C \exp \left(- \int \alpha(s, y') dy' \right), \quad (12)$$

where (s, y') are the coordinates of a point on the straight line S–R and $\alpha(P)$ denotes some average value of $\alpha(\omega; P)$ in the frequency range of the chirp pulse. This assumption is justified if equation (5), with $\eta = 0$, provides a satisfactory approximation. In addition, the constant C coincides with that given in equation (11).

The exponential dependence on the attenuation constant as well as the need of subtracting the effect of the bolus surrounding the body of interest suggests to define the CP-MCT data in the following way:

$$g_\theta(s) = \ln M_\theta(s) - \ln M_{b,\theta}(s), \quad (13)$$

where $M_{b,\theta}(s)$ are the raw data obtained, for instance, by means of a calibration procedure which consists in extracting the body from the bolus and collecting the corresponding CP-MCT data. For a fixed θ and varying s , this equation defines the CP-MCT *projection in the direction* θ .

Now, since the bolus consists of a homogeneous medium with uniform attenuation constant α_b , $M_{b,\theta}(s)$ is given by equation (11). If we introduce the *contrast function*

$$c(P) = \alpha_b - \alpha(P), \quad (14)$$

and its *Radon projection in the direction* θ

$$p_\theta(s) = \int c(s, y') dy', \quad (15)$$

then, by inserting equations (12) and (11) into equation (13), we get

$$g_\theta(s) = p_\theta(s). \quad (16)$$

In conclusion, if the approximations introduced in this section are valid, then the CP-MCT projections are approximately given by the corresponding Radon projections of the contrast function. We remark that this function is zero in the domain occupied by the bolus, is positive in the points where the body is *less* absorbing than the bolus and is negative in the points where the body is *more* absorbing than the bolus.

However, the CP-MCT sinograms look like blurred versions of the typical x-ray sinograms [7]. According to the modified linear model which accounts for this blurring [7], the CP-MCT projection of a phantom, $g_\theta(s)$, is related to its Radon projection, $p_\theta(s)$, by the linear relation

$$g_\theta(s) = \int R(s - s') p_\theta(s') ds', \quad (17)$$

where $R(s)$ is the PSF of the imaging system. An exhaustive description and an experimental validation of this model are given in [8, 9].

3. Numerical simulations

A quantitative analysis of the implications of the linear model requires the use of numerical simulations. Therefore, we need a code for generating CP-MCT raw data and a code for image reconstruction.

3.1. Raw data generation

A code for raw data generation can be based on an FD-TD code for simulating microwave propagation through the CP-MCT scanner. However, chirp waveforms are not suited for FD-TD time excitation because of the large value of the sweep time and the fast oscillatory behaviour of the chirp signal; as a consequence, a direct computation of the field at the receiving antenna is too heavy from the computational point of view.

For this reason, we have integrated the FD-TD code with a computational module implementing a method referred to as *after-effect function method* (A-EFM) [11, 12]. This method consists essentially in computing the transfer function of the medium (obtained by exciting, for instance, the transmitting antenna with the derivative of a suitable Gaussian function) and in multiplying this function by the Fourier transform of the chirp signal. Moreover, the code must implement simulation of the mixing and filtering procedures as well as background estimation and subtraction.

In our simulations, we have adopted a chirp signal with unit amplitude, minimum and maximum frequency of 1 and 2 GHz, respectively, and a sweep time $T_S = 9.09 \times 10^{-7}$ s. Moreover, the computation of the transfer function is accomplished by using, as input signal, a TM-polarized field whose dependence on time is given by the time derivative of a Gaussian function with standard deviation 2.15×10^{-10} s. The two antennas are assumed to be at a distance $d = 0.141$ m.

3.2. Image reconstruction

As already remarked in the introduction, image reconstruction based on the blurred linear model requires two steps: the first is a deconvolution of the raw data based on an estimate of the PSF and the second is standard FBP.

About the first step, the basic ingredient is the computation of the PSF. A method is proposed in [8]. However, not all details needed for implementing this computation are given in that paper and for this reason they are provided in the appendix. In addition, we need a deconvolution method.

Since, in the particular cases considered in the next section, we focus on bodies less absorbing than the surrounding bolus, the contrast function is non-negative and we can use the deconvolution method proposed in [8], namely the iterative method known as *projected Landweber method* with non-negativity constraint (see [13] for an introduction).

This reconstruction method is based on the validity of the model given in equation (17). Therefore, a check of this model can be obtained not only by comparing the result of the n th iteration $p^{(n)}(s)$ with the Radon projection $p(s)$ defined in equation (15), but also by verifying that the reconstructed $p^{(n)}(s)$ is able to reproduce the data g provided by the FD-TD computation. To this purpose, at each iteration, we compute the so-called *relative discrepancy* which is given by

$$\epsilon^{(n)} = \frac{\|R * p^{(n)} - g\|_2}{\|g\|_2}, \quad (18)$$

where $\|\cdot\|_2$ denotes the L^2 -norm. Since in our simulations we do not add noise to the data computed by means of FD-TD, the value of this quantity is an estimate of the error due to the model used for approximating the CP-MCT data.

4. Quantitative analysis of the linear model

The purpose of this section is to verify that, in the low-contrast case, if we apply the blurred linear model to CP-MCT raw data we can deduce quantitative information about the contrast function of the body. We mainly consider bodies with simple geometry in order to reduce the computational time in the use of FD-TD.

4.1. Centred cylinders

We consider a homogeneous cylinder with section Ω , radius a and uniform attenuation constant α_c , placed in the centre of the imaging region. If the cylinder is surrounded by a bolus with attenuation constant α_b , then the contrast function is zero outside Ω and given by $c = \alpha_b - \alpha_c$ inside Ω . As is obvious, the Radon projections of this phantom do not depend on θ and, if we denote by $p(s)$ their common value, it is well known that we have $p(s) = 2c\sqrt{a^2 - s^2}\chi_a(s)$, with $\chi_a(s)$ being the characteristic function of $[-a, a]$.

Since we assume space invariance of the PSF, also the corresponding CP-MCT projections do not depend on θ . If we insert the expression of $p(s)$ into equation (17) we get a formula leading to the following observations. First, for a fixed s , the corresponding value of the projection depends linearly on the contrast c ; second, the position of the zeros of $g(s)$ depends on the size of the cylinder but not on its contrast. It follows that for a fixed value of the radius and different values of the contrast, the zeros of the CP-MCT projections must fall on the same places.

The CP-MCT projections of cylindrical phantoms, all with radius $a = 0.02$ m but with different attenuation constants, have been computed by means of our FD-TD code, assuming that they are immersed in a bolus with permittivity $\epsilon_b = 73.9$ and conductivity $\sigma_b = 1.77$ S m⁻¹, which are the electrical parameters at 1.5 GHz of a saline solution with concentration 0.69% and temperature of 32°C. The corresponding value of the attenuation constant is $\alpha_b = 38.79$ m⁻¹. Moreover the phase velocity is 3.49×10^7 ms⁻¹, so that the delay time is $T_D = 4.04 \times 10^{-9}$ s. We also remark that in the frequency range between 1 and 2 GHz the variations of permittivity, as a function of the frequency, are smaller than 1% while those of conductivity and attenuation constant are of the order of 15% (we use the values given in [8]). Lastly, the value of the parameter η , defined in equation (3), is about 0.186.

The value of the permittivity of the cylinder has been set to $\epsilon_c = 74.5$ and the attenuation constant has been changed by only changing the conductivity. In such a way we have produced cylinders with a contrast with respect to the bolus ranging from 0 to $\pm 100\%$.

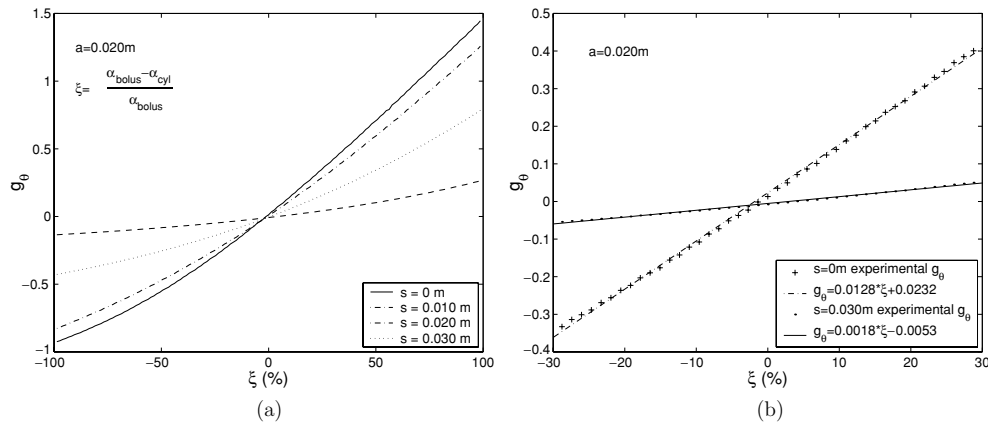


Figure 2. (a) FD-TD values of the CP-MCT projections of centred cylinders with the same radius and increasing contrast: the values of the projections, for four different positions s of the S–R pair, are given as a function of the relative contrast $\xi = c/\alpha_b$, with $c = \alpha_b - \alpha_c$. (b) FD-TD values of $g(s)$ and corresponding linear fits in the range $-30\% \leq \xi \leq 30\%$ for two different values of s .

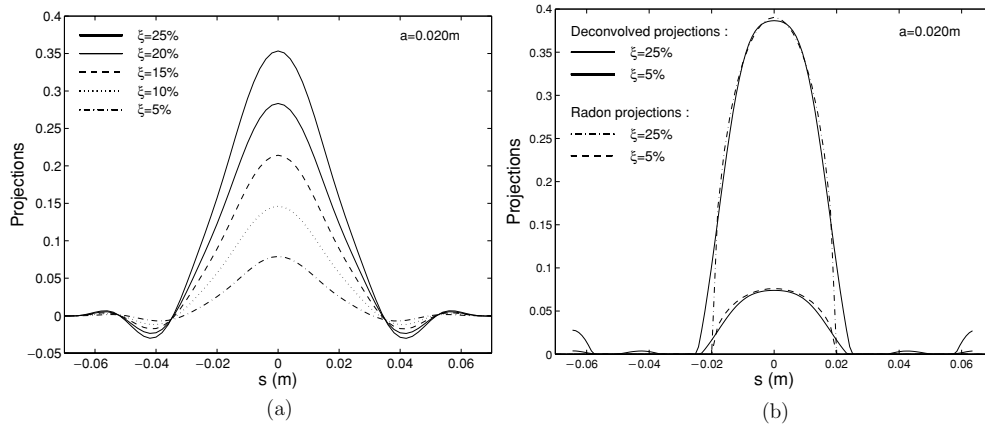


Figure 3. (a) CP-MCT projections of centred cylinders with fixed radius $a = 0.02$ m and five different contrast values. The position of the zeros does not depend on the contrast. (b) Deconvolution of the CP-MCT projections plotted in (a) and corresponding to 25% and 5% contrast. The deconvolved projections are compared with the corresponding Radon projections.

In figure 2(a), we plot the values of the CP-MCT projections $g(s)$ as a function of the relative contrast $\xi = c/\alpha_b$, for four different positions of the source–receiver pair (i.e., four different values of s). This plot demonstrates that linearity holds true in the range $-30\% \leq \xi \leq 30\%$, as confirmed by figure 2(b) where linear fits are superimposed to the computed values of $g(s)$ for the two limit values of s in figure 2(a). We point out that zero contrast in the attenuation constant corresponds to different electrical parameters of bolus and phantom. Since the difference in permittivity is kept fixed, this is compensated by a difference in conductivity. More precisely, the conductivity of the cylinder is $\sigma = 1.78$.

In figure 3(a), we plot the CP-MCT projections as functions of the s -variable for five different values of the contrast ξ . The fact that the positions of the zeros of $g(s)$ do not change

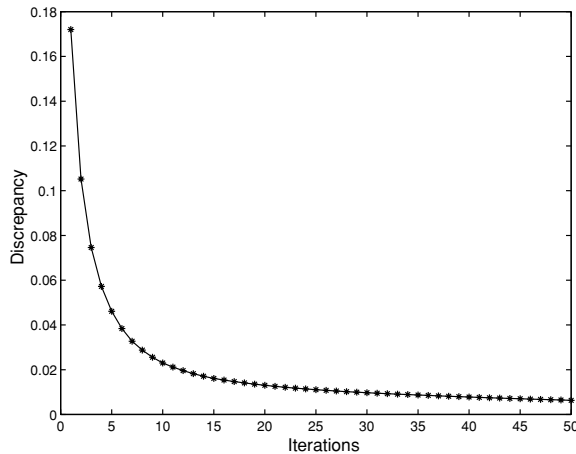


Figure 4. Behaviour of the discrepancy function as a function of the number of iterations. The curve refers to the case of 25% contrast.

with the contrast is verified as we predicted above. Moreover, an inspection of this figure provides a very interesting result. Indeed, the value of the Radon projection for $s = 0$ is given by $p(0) = 2ca$ and, by using the values of the contrast function, for the five cylinders of figure 3(a) one finds values ranging from 0.39, in the 25% case, to 0.078, in the 5% case, values remarkably close to the maximum values of the CP-MCT projections plotted in the figure, i.e. $g(0)$.

Next we applied the deconvolution method described at the beginning of the section. The PSFs corresponding to the correct values of the contrast (and normalized to unit area) were computed by means of the method given in [8]. Using 25 Landweber iterations, the deconvolved CP-MCT projections are in remarkable agreement with the corresponding Radon projections. In figure 3(b), we plot the results corresponding to the two extreme cases, namely 25% and 5% contrast. Except for small side lobes, we find a very good quantitative estimation of both the values of the Radon projections and the radius of the cylinder. An inspection of the figure indicates a few per cent error in the estimation of the radius, and such a good result is mainly due to the beneficial effect of the non-negativity constraint assured by the projected Landweber method.

Finally, in figure 4 we plot, as a function of the number of iterations, the relative discrepancy defined in equation (18). This quantity decreases to values smaller than 1%, indicating a very good agreement between the CP-MCT projection and the linear model.

4.2. Co-axial centred cylinders

The possibility of quantitative evaluation of the attenuation contrast by a processing of CP-MCT projections based on the linear model, at least in the low-contrast case, can be confirmed by investigating a more complex phantom. It consists of two centred co-axial cylinders, with radius a and b respectively, and $a > b$. We assume that the internal cylinder has a uniform attenuation constant corresponding to a contrast c_b with respect to the bolus; analogously, the surrounding cylinder has a (different) attenuation constant corresponding to a contrast c_a . Moreover, we assume $0 < c_b < c_a$. Also in such a case we have only one Radon

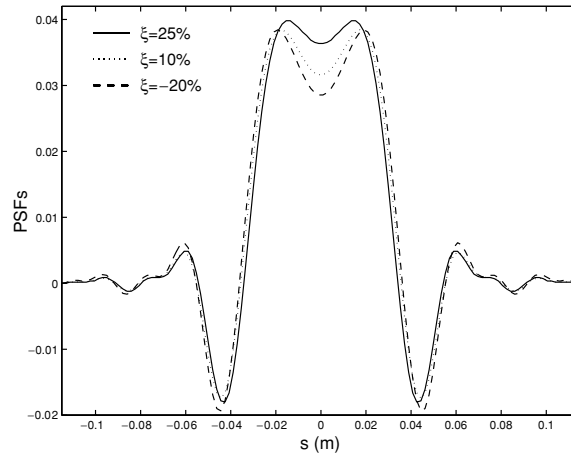


Figure 5. Plot of the three PSFs corresponding to the case of two co-axial cylinders.

projection given by

$$p(s) = \begin{cases} 2c_a\sqrt{a^2 - s^2} - 2c_b\sqrt{b^2 - s^2}, & |s| \leq b \\ 2c_a\sqrt{a^2 - s^2}, & b < |s| \leq a. \\ 0, & |s| > a \end{cases} \quad (19)$$

We have performed an FD-TD simulation for computing the corresponding CP-MCT projection in the following case: external bolus with the same electrical parameters of subsection 4.1; an external cylinder with radius $a = 0.04$ m and a positive contrast with respect to the bolus of 25% (hence less absorbing than the bolus), obtained as in subsection 4.1; an internal cylinder with radius $b = 0.01$ m, also less absorbing than the bolus, but with a contrast with respect to the bolus of 10% (hence with a negative contrast with respect to the external cylinder of -20%). In such a situation we have three PSFs, which are plotted in figure 5; all are normalized to unit area). The full line is the PSF of the external cylinder surrounded by the bolus, the dotted line that of the internal cylinder, also surrounded by the bolus and, finally, the dashed line that of the internal cylinder surrounded by the external one.

In figure 6(a), we plot the result of the FD-TD computation; if we compare with figure 3(a) we see that the presence of the internal cylinder is indicated by a small modification of the structure of the central lobe. This projection has been deconvolved using the three PSFs of figure 5; the best result has been obtained with the PSF of the external cylinder relative to the bolus and this result is shown in figure 6(b). The relative discrepancy is of the order of 5%, a number which shows again a good agreement with the linear model.

In figure 6(b), we also plot the Radon projection of the two cylinders and the quantitative agreement between the deconvolved CP-MCT projection and the Radon projection is fairly good. We point out that the estimate of the radius of the external cylinder is quite accurate, while the radius of the internal one is not precisely defined and is likely overestimated. The explication of this result resides on the fact that the estimation of the external radius is improved by the non-negativity constraint, as we already remarked in subsection 4.1, while in the internal region the non-negativity constraint is not active. As a consequence, the blurring of the CP-MCT projection is not completely removed by the deconvolution process.

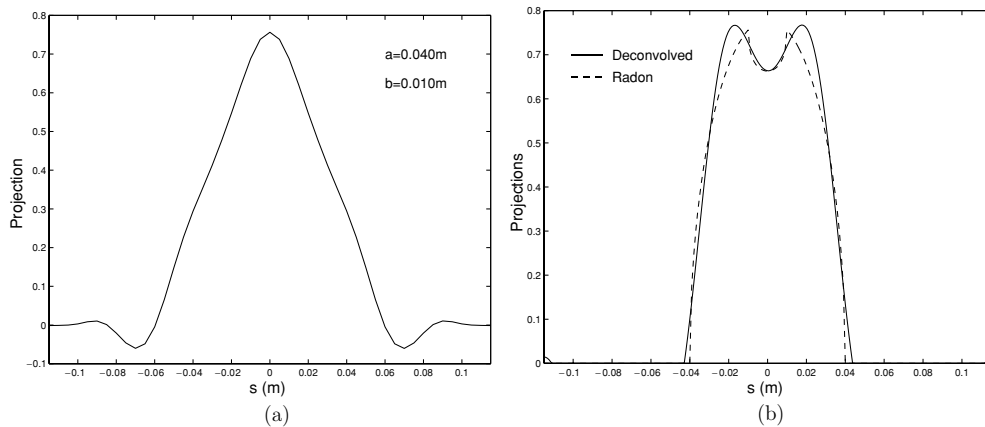


Figure 6. (a) CP-MCT projection of the two coaxial cylinders. (b) Deconvolution of the CP-MCT projection plotted in (a) obtained by means of the PSF of the external cylinder and 25 iterations of the projected Landweber method. The deconvolved projection is compared with the corresponding Radon projection.

4.3. Off-centre cylinders

The good quantitative accuracy obtained in the previous cases may be due not only to the beneficial effect of the non-negativity constraint but also to the symmetry of the phantoms we have considered. Therefore, we have performed a numerical simulation with a non-centred cylinder. In such a case one must compute different projections corresponding to different angles of view.

We have considered one of the cases of subsection 4.1, namely a bolus with the same electrical parameters and a cylinder with radius $a = 0.02$ m and a 25% contrast with respect to the bolus; but now the centre of the cylinder is at a distance of 0.015 m from the centre of the imaging region. We have computed 36 projections between 0° and 180° , and we have verified in a few cases that the projections corresponding to directions θ and $\theta + \pi$ are almost identical (another consequence of the linear model). Next, the CP-MCT projections have been deconvolved using the PSF corresponding to the electrical parameters of cylinder and bolus. Three of the deconvolved projections are displayed in figure 7(a).

A comparison with figure 3(b) shows that now the contrast is slightly overestimated at the centre of the cylinder as well as the radius. This remark also applies to the projection at 90° , that is symmetric, as the projection of a centred cylinder. The reason of this effect is not clear even if, of course, the two situations are not identical because, now, the two antennas are not at the same distance from the centre of the cylinder. For these reasons and also because the number of projections is small, the 2D reconstruction obtained by means of FBP is not very accurate. In figure 7(b), we plot the cut of the reconstructed cylinder along the line through its centre and orthogonal to the line joining its centre with the centre of the imaging region. An artefact at the centre of the cylinder has to be remarked upon. Anyway, the estimate of the radius looks satisfactory.

5. Concluding remarks

In this paper we have investigated the assumptions leading to the linear model used in the processing of CP-MCT data. It is shown that the model is the result of very crude

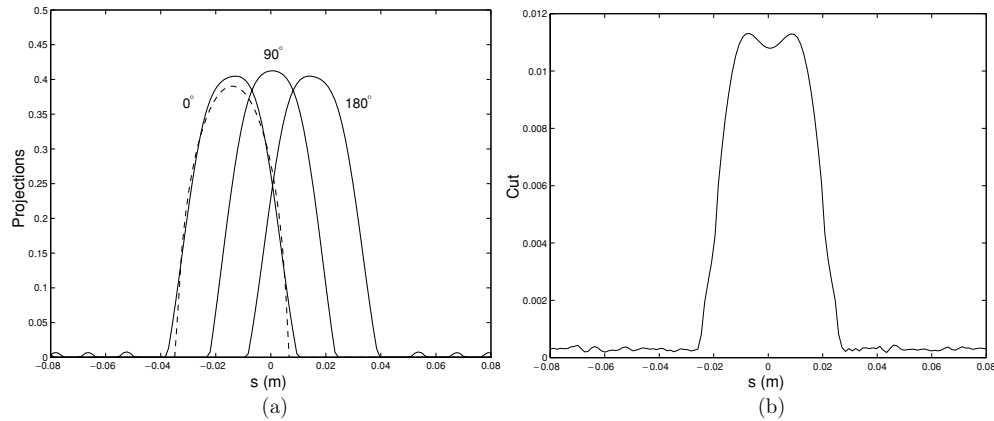


Figure 7. (a) Deconvolved CP-MCT projections of the off-centre cylinder. The projections corresponding to 0° , 90° and 180° are displayed. In the case of the projection at 0° the corresponding Radon projection (dashed line) is also shown. (b) Cut of the reconstructed cylinder along the line through its centre and orthogonal to the line joining its centre with the centre of the imaging region.

approximations on the data provided by the application of MTDS to CP-MCT. These approximations derive from strong assumptions on the electrical properties of the body to be investigated. Since, according to the model, CP-MCT is a technique providing maps of the attenuation constant, this parameter must weakly depend on the frequency in the range between 1 and 3 GHz and must not suffer strong variations within the body to be imaged. In other words, CP-MCT is a technique which works well in the low-contrast case.

Anyway, our numerical simulations show that in the case of phantoms with a simple geometry and a weak contrast with respect to the bolus the model allows a rather accurate quantitative estimate of the contrast function. Such a result is a bit surprising due to the crudeness of the approximations. It suggests to look for practical situations where CP-MCT could provide not only a fast but also an accurate reconstruction of the map of the attenuation constant.

Appendix

The PSF, defined as the CP-MCT projection of a small cylinder placed in the centre of the imaging region, can be derived from a scattering theory approach [8]. The results provided by this approximate method have been confirmed by FD-TD computations as well as by an analysis of experimental data [9, 12]. In this appendix, we give additional details which are useful for understanding and implementing our computational method.

Let us denote by $u(s; t)$ the signal at the receiving antenna when the S–R pair S is at a (signed) distance s from the origin (see figure 1), and S is fed up by the chirp signal given in equation (6). In [8], the computation of the PSF is based on the computation of $\hat{u}(s; \omega)$ provided by the Born approximation (justified by the smallness of the cylinder). If we denote by k , k_b and k_0 the wavenumbers, respectively, of the cylinder, bolus and empty space ($k_0 = \omega/c$), then the result is the following:

$$\hat{u}(s; \omega) = \hat{c}(\omega) \hat{v}(s; \omega), \quad (\text{A.1})$$

$$\hat{v}(s; \omega) = \frac{i}{4} \left\{ \sqrt{\frac{2}{\pi}} e^{-i\pi/4} \frac{e^{ik_b d}}{\sqrt{k_b d}} + a^2 k_0 (k_b - k) \frac{e^{ik_b \sqrt{d^2 + 4s^2}}}{k_b \sqrt{d^2 + 4s^2}} \right\}. \tag{A.2}$$

The first term in (A.2) is the contribution of the bolus and the second one the contribution of the small cylinder of radius a (first-order term in the expansion in powers of $(k_0 a)^2$).

The next step is the computation of the convolution product

$$\hat{h}(s; \omega) = \frac{1}{2\pi} (\hat{c} * \hat{u})(s; \omega). \tag{A.3}$$

Its maximum value, corresponding to the beating frequency, provides the result of the mixing/filtering procedure. Finally, by taking the logarithm of this result and subtracting the contribution of the bolus, we obtain the PSF $R(s)$, that is normalized to unit area.

Therefore, the crucial step is the computation of the convolution product and, to this aim, we need an approximate computation of $\hat{c}(\omega)$:

$$\hat{c}(\omega) = A \int_0^{T_S} \sin \left(\omega_1 t + \frac{1}{2} K t^2 \right) e^{i\omega t} dt. \tag{A.4}$$

By using the Euler formula for the sine function and the two identities

$$\omega_1 t + \frac{1}{2} K t^2 \pm \omega t = \left(\sqrt{\frac{K}{2}} t \pm \sqrt{\frac{2}{K}} \frac{\omega \pm \omega_1}{2} \right)^2 - \left(\sqrt{\frac{2}{K}} \frac{\omega \pm \omega_1}{2} \right)^2 \tag{A.5}$$

we obtain

$$\hat{c}(\omega) = \frac{A}{2i} \left\{ e^{-i \frac{(\omega + \omega_1)^2}{2K}} \int_0^{T_S} e^{i w_1^2} dt - e^{-i \frac{(\omega - \omega_1)^2}{2K}} \int_0^{T_S} e^{i w_2^2} dt \right\}, \tag{A.6}$$

where

$$w_1 = \sqrt{\frac{K}{2}} t + \sqrt{\frac{2}{K}} \frac{\omega_1 + \omega}{2}, \quad w_2 = \sqrt{\frac{K}{2}} t - \sqrt{\frac{2}{K}} \frac{\omega - \omega_1}{2}. \tag{A.7}$$

By using w_1 and w_2 as new integration variables, respectively, in the first and second integrals, and the relationship $K T_S = \omega_2 - \omega_1$, we can write

$$\hat{c}(\omega) = \frac{A}{2i} \sqrt{\frac{2}{K}} \left\{ e^{-i \frac{(\omega + \omega_1)^2}{2K}} \int_{\frac{\omega + \omega_1}{\sqrt{2K}}}^{\frac{\omega_2 + \omega}{\sqrt{2K}}} e^{i w^2} dw - e^{-i \frac{(\omega - \omega_1)^2}{2K}} \int_{\frac{\omega_1 - \omega}{\sqrt{2K}}}^{\frac{\omega_2 - \omega}{\sqrt{2K}}} e^{i w^2} dw \right\}. \tag{A.8}$$

The values of the two Fresnel integrals in (A.8) are negligible for ω respectively outside the intervals $[-\omega_2, -\omega_1]$ and $[\omega_1, \omega_2]$. Furthermore, in these two intervals the two integrals oscillate slightly around the constant value $\sqrt{\pi}$. Therefore,

$$\hat{c}(\omega) \simeq \hat{c}^{(+)}(\omega) + \hat{c}^{(-)}(\omega), \tag{A.9}$$

where

$$\hat{c}^{(\pm)}(\omega) = \mp \frac{A}{2i} \sqrt{\frac{2\pi}{K}} e^{\pm i \frac{(\omega \mp \omega_1)^2}{2K}} \chi^{(\pm)}(\omega), \tag{A.10}$$

and $\chi^{(\pm)}(\omega)$ denote respectively the characteristic functions of the intervals $[\omega_1, \omega_2]$ and $[-\omega_2, -\omega_1]$. With this approximation, and the representation (A.1) of $\hat{u}(s; \omega)$, the convolution product (A.3) becomes

$$\hat{h}(s; \omega) \simeq \frac{1}{2\pi} [\hat{c}^{(-)} * \hat{c}^{(+)} \hat{v}](\omega) + \frac{1}{2\pi} [\hat{c}^{(+)} * \hat{c}^{(-)} \hat{v}](\omega), \tag{A.11}$$

where the two terms $\hat{c}^{(-)} * \hat{c}^{(-)} \hat{v}$ and $\hat{c}^{(+)} * \hat{c}^{(+)} \hat{v}$, with support respectively in $[-2\omega_2, -2\omega_1]$ and $[2\omega_1, 2\omega_2]$, have been neglected, since they are zero at $\omega = \omega_B$.

From the expressions (A.10) and (A.2) for $\hat{c}^{(+)}$, $\hat{c}^{(-)}$ and $\hat{v}(\omega, s)$ respectively and the approximations (5) for the attenuation and phase constants into (A.2), we obtain, for the two integrals of equation (A.11), expressions which can be computed analytically if the second mean value theorem is used in order to extract the non-oscillating terms. In such a way, one can easily show that the first term on the right-hand side of (A.11) has a maximum around $\omega = -\omega_B$, while the second term has a maximum around $\omega = \omega_B$. Since the first term is negligible around ω_B with respect to the second one, the final approximate expression for the convolution product is

$$\hat{h}(s; \omega) = \frac{A^2}{4K} e^{-\frac{i}{K}\omega\omega_1} e^{\frac{i}{2K}\omega^2} \int_{\omega_1}^{\omega_2-\omega} e^{\frac{i}{K}\omega\omega'} \hat{v}(s; -\omega') d\omega'. \quad (\text{A.12})$$

This integral can be computed numerically around ω_B . Then one can take the maximum of the modulus and apply the usual procedure for the computation of the projection.

References

- [1] Miyakawa M 1992 An attempt of microwave imaging of the human body by the chirp radar-type microwave CT *IEICE Trans.* **J-75-D-II** 1447–54
- [2] Miyakawa M, Watanabe D and Saitoh Y 1992 Imaging of temperature change by the improved chirp radar-type microwave computed tomography *IEE Trans.* **112** 494–99
- [3] Miyakawa M 1993 Tomographic measurement of temperature change in phantoms of the human body by chirp radar-type microwave computed tomography *Med. Biol. Eng. Comput.* **31** 31–6
- [4] Miyakawa M 1996 Microwave imaging: I. Microwave computed tomography *Non-invasive Thermometry of Human Body* ed M Miyakawa and J C Bolomey (Boca Raton, FL: CRC Press) pp 105–26
- [5] Jacobi J H and Larsen L E 1978 Microwave interrogation of dielectric targets: Part 2. By microwave time delay spectroscopy *Med. Phys.* **5** 509–18
- [6] Fhager A and Persson M 2005 Comparison of two image reconstruction algorithms for microwave tomography *Radio Sci.* **40** 2004RS003105, RS3017
- [7] Bertero M, Miyakawa M, Boccacci P, Conte F, Orikasa K and Furutani M 2000 Image restoration in chirp-pulse microwave CT (CP-MCT) *IEEE Trans. Biomed. Eng.* **47** 600–9
- [8] Bertero M, Conte F, Miyakawa M and Piana M 2001 Computation of the response function in chirp-pulse microwave computerized tomography *Inverse Problems* **17** 485–500
- [9] Miyakawa M, Orikasa K, Bertero M, Boccacci P, Conte F and Piana M 2002 Experimental validation of a linear model for data reduction in chirp-pulse microwave CT *IEEE Trans. Med. Imag.* **21** 385–95
- [10] Miyakawa M, Kai K and Che R D 1998 Fan beam based high speed imaging of the chirp radar-type microwave computed tomography *Proc. PIERS 98, PIERS 1998 (Nantes, 13–17 July 1998)*
- [11] Furutani M, Miyakawa M, Hoshina S, Kanai Y and Ishii N 1998 A numerical analysis of the tomographic imaging of the chirp radar-type microwave computed tomography—computation of the projection data based on a transfer function method *IEICE Tech. Rep.* AP98 **110** 13–18
- [12] Miyakawa M, Orikasa K and Bertero M 2002 Evaluation of the response function and its space dependence in chirp-pulse microwave computed tomography (CP-MCT) *IEICE Trans. Inf. Syst.* **E85-D** 52–9
- [13] Bertero M and Boccacci P 1998 *Introduction to Inverse Problems in Imaging* (Bristol: Institute of Physics Publishing)